Annals of Mathematical Sciences and Applications
Volume 5, Number 1, 7–39, 2020

Simulation of tumor-induced angiogenesis by an HOC approach

Jiten C. Kalita*, Shubham Goyal, and Utkarsh Dixit

Angiogenesis is one of the main processes of vascularization resulting in the formation of capillary sprouts in response to externally supplied chemical stimuli. Till date, most of the numerical works simulating the process of angiogenesis has been carried out by lower order accurate schemes like Euler explicit, which may not be good enough to predict the physiological process correctly because of their over diffusive nature. In the present work, we propose a fourth order spatially accurate and second order temporally accurate finite difference scheme for the equations governing the process of angiogenesis from an existing continuous model. For the discrete counterpart of the same model, the coefficients representing the probability density is computed by our high order compact (HOC) data. The proposed scheme is employed to carry out computation of the evolution of endothelial cell migration for three cases: the first two corresponds to the advancement of the density of endothelial-cell in time and space mirroring the migration of the endothelial-cells from the parent vessel towards a tumor cell source in the shape of a line, one in the presence of haptotaxis and the other without it. The last deals with the same with a circular tumor cell source with haptotaxis. We also demonstrate that simulation resulting from a lower order accurate scheme might lead to misrepresentation of the physiological process, particularly in the later stages. Contrary to this, in each of the cases, our HOC simulations match excellently with earlier benchmark numerical and some experimental results for all stages of the process, thus confirming the robustness and efficiency of the proposed numerical scheme.

AMS 2000 subject classifications: Primary 92Bxx, 92C17; secondary 76M20.

Keywords and phrases: Angiogenesis, Tumor, Sprouting, High-order-compact, Cell migration.

*Corresponding author. ORCID: 0000-0001-5527-5704.

1. Introduction

Angiogenesis (*syn* neovascularization) [1, 3, 9, 13, 14, 15, 22, 35, 36, 44, 45, 53, 54, 56] is the sprouting of fresh blood vessels and capillary beds from existing vessels, which plays a fundamental role in embryonic development, resolution of inflammation, and onset of neoplasia. Angiogenesis is linked to certain pathologies – e.g., cancer, diabetic retinopathy, rheumatoid arthritis, etc. One can also find its occurence during tissue repair in adult mammals, albeit in a controlled manner [3]. On the other hand, Falkman *et al.* [14, 15] have reported that uncontrolled or excessive blood-vessel formation is vital for tumorigenesis and manifests in abnormal *neovascularization* of the eye, arthritis, duodenal ulcers, and in many more physiological processes such as myocardial infarction. However, in all the cases, the well-ordered sequence of events typical of angiogenesis is the same: it starts with the rearrangement and migration of endothelial cells from a preexisting vasculature and then culminates in the formation of a widespread network of fresh capillaries [35]. The progress of tumor induced angiogenesis occurs mainly through the following sequence of three events:

- The process of angiogenesis starts with the secretion of certain chemicals by the carcinogenic cells of a solid tumor into the surrounding tissues; they are popularly known in abbreviated form as TAF, standing for tumor angiogenic factors [15].
- Subsequently, diffusion of the TAF takes place through the tissue space leading to the formation of a chemical gradient between the tumor and any existing vasculature.
- On reaching any neighboring blood vessels situated on their edges, the endothelial cells are first induced to damage the parent venule basement membranes and then wander towards the tumor through the damaged membrane.

The isolation of several TAF such as vascular endothelial growth factor (VEGF), acidic and basic fibroblast growth factor (aFGF, bFGF), angiogenin and others [15], and subsequent discovery of endothelial cell receptors for these proteins have been extensively reported in literature [11, 16, 20, 21, 23, 38, 40, 41, 43]. Experiment shows that the disruption of these receptors has a direct bearing on the final structure of the capillary network [12]. Hence, the study of the movement of endothelial cells during angiogenesis has generated a renewed interest amongst the mathematical biology community [1, 9, 36, 26].

Initially, endothelial cells have a chemotactic response to the aforementioned angiogenic factors [49], which initiates the movement of cells towards the tumor. Subsequently, tiny, claw-like capillary sprouts are formed by the accumulation of endothelial cells [10, 49] which continue to grow and move towards the tumor. The movement of the capillaries is usually determined by the motion of the foremost endothelial cell located at the sprout tip. The process of sprout extension continues further when the endothelial cells begin to multiply. The movement of the sprout tip and its consequent multiplication of sprout-wall cells lead to the formation of solid strands of endothelial cells amongst the extracellular matrix. The meandering of the cells through the extracellular matrix continues further; the matrix is made up of fibronectin, collagen fiber and interstitial tissues as well as other components [33]. The role of fibronectin, more specifically that of **haptotaxis** in the adhesion of cells to the extracellular matrix and the interplay of TAF with them in cell migration can be found in the studies of [6, 25, 26, 31, 37, 46, 48]. On the other hand the role of sprout branching and looping in spreading the capillary bed resulting in cell migration have been well documented in the studies of [44] and [39].

Mathematical modeling of tumor induced angiogenesis has attracted the attention of oncologists, biologists, the pharmaceutical industry and mathematicians alike in the last half of the century. A comprehensive discussion on this can be found in the work of Mantzaris *et al.* [36] and Valinova *et al* [54]. As would be seen in the subsequent sections, the modeling of angiogenesis involves solving a coupled system of partial differential equations one of which is of reaction-diffusion type and highly nonlinear. As such, it must be solved by numerical methods. A close look at the numerical studies on this topic over the years reveal that in most of the cases some standard lower order accurate schemes like Euler's explicit finite difference scheme [1, 13, 36] was used to discretize the governing equations. However, all these schemes are fraught with inherent implicit numerical diffusion and dispersion [2, 24] and the simulation resulting from these schemes may not represent the physiological phenomena accurately, specifically at the later part of the evolution. Moreover, because of stability issues, extremely smaller time steps are required for simulation.

In this context, it is imperative to explore the possibility of employing High Order Compact (HOC) [18, 19, 27, 28, 29, 32, 42, 51] scheme for the governing equations modelling angiogenesis and examine how this scheme behaves when applied to simulate the evolution of cell migration. The motivation behind embarking on a study such as the current one is to devise an HOC scheme for such equations. If a finite difference method utilizes no

more than one grid point away from the node about which finite difference approximations are taken, it is called a compact scheme. Along with this, if its spatial accuracy is $O(h^2)$ or more (h being the space step length), it is termed as an HOC method. The marriage between the higher order accuracy and the compactness of the difference stencils of the HOC methods yields high quality numerical solutions with greater computational economy. In the present work, we develop an HOC scheme mainly for the equation governing the motion of endothelial cell density; the scheme is implicit, second order accurate in time and fourth order accurate in space.

This paper is organized in the following way. In Section 2, we provide a brief discussion on the mathematical model being used, in Section 3, we give the details of development of the numerical scheme for the endothelial cell density equation, in Section 4, we provide a brief on the discrete model, Section 5 and 6 respectively deal with the numerical simulations with the continuous and discrete models, Section 7 with numerical issues and finally in Section 8, we summarize our achievements in conclusions.

2. The mathematical model used

In the existing literature, one can find a plethora of mathematical models developed over the years using different approaches. These models have evolved over the years by gradually incorporating more crucial features of angiogenesis induced by a tumor. Most of the earlier one of these models employed a deterministic framework in a continuum of one space dimension [5, 9, 34, 55]. Despite being capable of exhibiting several important features of angiogenesis, these models fell short in predicting the morphology and actual structure of the capillary network. In 1998, Anderson and Chaplain proposed a more realistic model of angiogenesis in two space dimensions [1] which utilizes a blend of the continuum and probabilistic (discrete) approaches, merging the respective strengths of each approach. It focuses on the three crucial variables involved in angiogenesis induced by a tumor that had been mentioned in Section 1, viz., endothelial cells, TAF and fibronectin. In the following, we provide a brief description on the coupled system of partial differential equations governing the phenomenon.

If the normalized endothelial-cell density per unit area is denoted by n, the TAF concentration by c and the fibronectin concentration by f, the equations governing this physiological phenomena reduce to

$$
(1)\qquad
\begin{aligned}
\frac{\partial n}{\partial t} &= D\nabla^2 n - \nabla\cdot\left(\frac{\chi}{1+\alpha c} n\nabla c\right) - \nabla\cdot(\rho n\nabla f)\\
\frac{\partial f}{\partial t} &= \beta n - \gamma n f\\
\frac{\partial c}{\partial t} &= \eta n c
\end{aligned}
$$

subject to the following no-flux condition

$$
(2)\qquad \xi\cdot\left(-D\nabla n + n\left(\frac{\chi}{1+\alpha c}\right)\nabla c + \rho\nabla f\right) = 0
$$

on the boundaries (ξ being a unit normal to the boundary), where it is assumed that the domain under consideration is a unit square.

The details of the derivation of the partial differential equations governing the physiological phenomena and their non-dimensionalisation along with the description of the constants and coefficients D, χ, α, ρ, β, γ, and η can be found in [1, 13, 36].

3. Solution of equations by HOC schemes

To solve the first equation in the system of eauations (1) governing endothelial-cell motion, we will frame an implicit, unconditionally stable higher order compact (HOC) difference scheme in the line of the one proposed in [28]. The scheme has a second-order temporal accuracy and a spatial accuracy of four. It is set on a stencil that utilizes nine and five points at the nth and $(n+1)$th time levels respectively and as such termed a (9,5) HOC scheme. It was seen to efficiently capture both transient and steady solutions of linear and non-linear convection-diffusion equations with Dirichlet as well as Neumann boundary conditions.

3.1. Introduction to higher order compact scheme for the continuous model

The unsteady two-dimensional (2-D) convection-diffusion equation for a transport variable ϕ in some continuous domain with suitable boundary conditions can be written as

$$
(3)\qquad a\frac{\partial\phi}{\partial t} - \nabla^2\phi + c\,(x,y,t)\frac{\partial\phi}{\partial x} + d\,(x,y,t)\frac{\partial\phi}{\partial y} + \varepsilon\,(x,y,t)\,\phi = g\,(x,y,t)
$$

where a is a constant, c and d are the convection coefficients, ε some potential function and g, a source term. This scheme is able to solve very

accurately and efficiently the transient 2-D convection-diffusion problems. Owing to a more compact difference stencil than the standard high order schemes coupled with its temporal accuracy, it is seen to be more CPU time-wise efficient than them.

3.2. The governing equation in the convection-diffusion format

On expanding and simplifying the expression of ∇^2 and ∇ of in the first equation in n of the set of equations (1), the resultant equation becomes

$$\begin{aligned}(4)\qquad \frac{\partial n}{\partial t} &= D\left(\frac{\partial^2 n}{\partial x^2}+\frac{\partial^2 n}{\partial y^2}\right)-\left(\frac{\chi}{1+\alpha c}\frac{\partial c}{\partial x}\right)\frac{\partial n}{\partial x}-\left(\frac{\chi}{1+\alpha c}\frac{\partial c}{\partial y}\right)\frac{\partial n}{\partial y}\\ &\quad-\left(\frac{\chi}{1+\alpha c}\frac{\partial^2 c}{\partial x^2}-\frac{\chi}{(1+\alpha c)^2}\left(\frac{\partial c}{\partial x}\right)^2\right.\\ &\quad\left.+\frac{\chi}{1+\alpha c}\frac{\partial^2 c}{\partial y^2}-\frac{\chi}{(1+\alpha c)^2}\left(\frac{\partial c}{\partial y}\right)^2\right)n\\ &\quad-\left(\rho\frac{\partial f}{\partial x}\right)\frac{\partial n}{\partial x}-\left(\rho\frac{\partial f}{\partial y}\right)\frac{\partial n}{\partial y}-\left(\rho\frac{\partial^2 f}{\partial x^2}+\rho\frac{\partial^2 f}{\partial y^2}\right)n\end{aligned}$$

On collecting the coefficients of $\dfrac{\partial n}{\partial x}$, $\dfrac{\partial n}{\partial y}$, n and rearranging, equation (4) reduces to

$$(5)\quad \tilde{a}\frac{\partial n}{\partial t}-\nabla^2 n+\tilde{c}\,(x,y,t)\frac{\partial n}{\partial x}+\tilde{d}\,(x,y,t)\frac{\partial n}{\partial y}+\tilde{\varepsilon}\,(x,y,t)n=\tilde{g}\,(x,y,t)$$

where $\tilde{a}$, $\tilde{c}$, $\tilde{d}$, $\tilde{\varepsilon}$ and $\tilde{g}$ are as follows:

$$\begin{aligned}\tilde{a} &= \frac{1}{D}\\ \tilde{c}\,(x,y,t) &= \frac{1}{D}\left(\frac{\chi}{1+\alpha c}\frac{\partial c}{\partial x}+\rho\frac{\partial f}{\partial x}\right)\\ \tilde{d}\,(x,y,t) &= \frac{1}{D}\left(\frac{\chi}{1+\alpha c}\frac{\partial c}{\partial y}+\rho\frac{\partial f}{\partial y}\right)\\ \tilde{\varepsilon}\,(x,y,t) &= \frac{1}{D}\left(\frac{\chi}{1+\alpha c}\frac{\partial^2 c}{\partial x^2}-\frac{\chi}{(1+\alpha c)^2}\left(\frac{\partial c}{\partial x}\right)^2\right.\\ &\quad+\left.\frac{\chi}{1+\alpha c}\frac{\partial^2 c}{\partial y^2}-\frac{\chi}{(1+\alpha c)^2}\left(\frac{\partial c}{\partial y}\right)^2\right)+\frac{1}{D}\left(\rho\frac{\partial^2 f}{\partial x^2}+\rho\frac{\partial^2 f}{\partial y^2}\right)\\ \tilde{g} &= 0\end{aligned}$$

3.3. Discretization

We consider the problem domain in a rectangular Cartesian framework and create a uniform mesh over it assuming that the uniform step lengths in the x- and y-directions are h and k respectively. Using the standard central difference approximation for the space derivative and forward-time approximation for the time derivatives, the first equation in (1) at the *(i, j)*th node can be discretized as

$$\begin{aligned} \left(\tilde{a}\delta_t^+ - \delta_x^2 - \delta_y^2 + \tilde{c}\delta_x + \tilde{d}\delta_y + \tilde{\varepsilon}\right) n_{ij} - \zeta_{ij} &= 0 \\ \delta_t^+ f_{ij} &= \beta n_{ij} - \gamma n_{ij} f_{ij} \\ \delta_t^+ c_{ij} &= -\eta n_{ij}\, c_{ij} \end{aligned} \tag{6}$$

where n_{ij} denotes $n(x_i, y_j)$, f_{ij} denotes $f(x_i, y_j)$, c_{ij} denotes $c(x_i, y_j)$; δ_x, δ_x^2 and δ_y, δ_y^2 are the first and second-order central difference operators along x- and y-directions respectively and δ_t^+ is the first-order forward difference operator for time. The truncation error ζ_{ij} with a uniform time step Δt is given by

$$\begin{aligned} \zeta_{ij} &= \left[\tilde{a}\frac{\Delta t}{2} + \frac{h^2}{12}\left(2\tilde{c}\frac{\partial^3 n}{\partial x^3} - \frac{\partial^4 n}{\partial x^4}\right) + \frac{k^2}{12}\left(2\tilde{d}\frac{\partial^3 n}{\partial y^3} - \frac{\partial^4 n}{\partial y^4}\right)\right]_{ij} \\ &+ O\left(\Delta t^2, h^4, k^4\right) \end{aligned} \tag{7}$$

Following the work of Kalita and Chhabra [28], we substitute ζ_{ij} from equation (7) to equation (6) and applying the same spatio-temporal approximations yields an $O\left(\Delta t^2, h^4, k^4\right)$ for equation (5) on a $(9, 5)$ stencil as

$$\begin{aligned} &\tilde{a}\left[1 + \left(\tfrac{h^2}{12} - \tfrac{\Delta t}{2\tilde{a}}\right)\left(\delta_x^2 - \tilde{c}_{ij}\delta_x\right) + \left(\tfrac{k^2}{12} - \tfrac{\Delta t}{2\tilde{a}}\right)\left(\delta_y^2 - \tilde{d}_{ij}\delta_y\right) + \tfrac{\Delta t}{2\tilde{a}}\varepsilon_{ij}\right]\delta_t^t n_{ij} \\ &\qquad + \left(-\alpha_{ij}\delta_x^2 - \beta_{ij}\delta_y^2 + C_{ij}\delta_x + D_{ij}\delta_y + E_{ij}\right) n_{ij} \\ &\qquad - \left(\tfrac{h^2+k^2}{12}\right)\left(\delta_x^2\delta_y^2 - \tilde{c_{ij}}\delta_x\delta_y^2 - \tilde{d_{ij}}\delta_x^2\delta_y - \tilde{\gamma_{ij}}\delta_x\delta_y\right) n_{ij} = 0 \end{aligned} \tag{8}$$

where α_{ij}, β_{ij}, C_{ij}, D_{ij}, E_{ij} and γ_{ij} are as follows:

$$\begin{aligned} \alpha_{ij} &= 1 + \frac{h^2}{12}\left(\tilde{c}_{ij}^2 - 2\delta_x\tilde{c}_{ij} - \tilde{\varepsilon}_{ij}\right) \\ \beta_{ij} &= 1 + \frac{k^2}{12}\left(\tilde{d}_{ij}^2 - 2\delta_y\tilde{d}_{ij} - \tilde{\varepsilon}_{ij}\right) \\ C_{ij} &= \left[1 + \frac{h^2}{12}\left(\delta_x^2 - \tilde{c}_{ij}\delta_x\right) + \frac{k^2}{12}\left(\delta_y^2 - \tilde{d}_{ij}\delta_y\right) + \frac{\Delta t}{2}\delta_t^-\right]\tilde{c}_{ij} \end{aligned}$$

$$
\begin{aligned}
&+ \quad \frac{h^2}{12}\left(2\delta_x - \tilde{c}_{ij}\right)\tilde{\varepsilon}_{ij} \\
D_{ij} &= \left[1 + \frac{h^2}{12}\left(\delta_x^2 - \tilde{c}_{ij}\delta_x\right) + \frac{k^2}{12}\left(\delta_y^2 - \tilde{d}_{ij}\delta_y\right) + \frac{\Delta t}{2}\delta_t^-\right]\tilde{d}_{ij} \\
&+ \quad \frac{k^2}{12}\left(2\delta_y - \tilde{d}_{ij}\right)\tilde{\varepsilon}_{ij} \\
E_{ij} &= \left[1 + \frac{h^2}{12}\left(\delta_x^2 - \tilde{c}_{ij}\delta_x\right) + \frac{k^2}{12}\left(\delta_y^2 - \tilde{d}_{ij}\delta_y\right) + \frac{\Delta t}{2}\delta_t^-\right]\tilde{\varepsilon}_{ij} \\
\tilde{\gamma}_{ij} &= \frac{2}{h^2 + k^2}\left(h^2\delta_x\tilde{d}_{ij} - k^2\delta_y\tilde{c}_{ij}\right) - \tilde{c}_{ij}\tilde{d}_{ij}
\end{aligned}
$$

Equation (8) in single matrix form can be written as

$$A\phi^{(n+1)} = f\left(\phi^n\right). \tag{9}$$

The coefficient matrix A above is an asymmetric pentadiagonal sparse matrix. We have employed biconjugate gradient stabilized method (BiCGStab) [30, 50] with algebraic multigrid as preconditioner to solve the (9) using the LIS library [57].

A forward time (FT) approximation is used to discretize the second equation of (1) to solve the concentration of fibronectin (f):

$$\delta_t^+ f_{ij} = \beta n_{ij} - \gamma n_{ij} f_{ij} \tag{10}$$

writing equation (10) in (n+1)th and (n)th time level, we get

$$f_{ij}{}^{(n+1)} = f_{ij}{}^{(n)} + \Delta t\left(\beta n_{ij}{}^{(n)} - \gamma n_{ij}{}^{(n)} f_{ij}{}^{(n)}\right) \tag{11}$$

Likewise, in order to solve the concentration of TAF (c), the third equation of (1) is discretized as:

$$c_{ij}{}^{(n+1)} = c_{ij}{}^{(n)} + \Delta t\left(-\eta n_{ij}{}^{(n)} c_{ij}{}^{(n)}\right) \tag{12}$$

We now move to the discretization of the no flux condition given by equation (2). Note that ξ represents a unit outward normal vector chosen suitably in accordance with the location of the boundary. For the top and bottom boundaries, ξ is $\hat{j}$, a unit vector parallel to y-axis, so that the no-flux boundary condition at the top and bottom reduces to:

$$\left(-D\frac{\partial n}{\partial y} + n\left(\frac{\chi}{1 + \alpha c}\right)\frac{\partial c}{\partial y} + \rho\frac{\partial f}{\partial y}\right) = 0 \tag{13}$$

Since the approximation of the time derivative of f and c involve only the $(i,j)^{\text{th}}$ spatial point, the approximation of the no-flux boundary condition is rendered only for the n-equation. As such equation (13) can be written as

$$\frac{\partial n}{\partial y} = f_1(x,y), \tag{14}$$

where $f_1(x,y)$ is known. At the bottom boundary (denoted by the index b), we approximate the values of n arising out of this Neumann boundary condition by the fifth order backward difference formula (see [2]):

$$n_{i,b} = \frac{1}{25}\left[48n_{i,b+1} - 36n_{i,b+2} + 16n_{i,b+3} - 3n_{i,b+4} - 12h\left(f_1\right)_{i,b}\right] + O(h^5),$$

where the values of the spatial derivatives appearing in the expression for f_1 can again be approximated by using a similar formula as above with slight adjustments. Approximations to the other no-flux boundary conditions could be carried out in a similar way.

In the next section, we briefly describe the discrete mathematical model used in the simulation of the movement of capillary sprout networks of endothelial cells.

4. The discrete mathematical model

Anderson and Chaplain [1] developed an innovative approach for the discrete mathematical model of angiogenesis induced by tumor that paved the way for both qualitative and quantitative comparison with its corresponding in vivo experimental counterparts. It involves firstly the discretization of the partial differential equation governing the rate of change of endothelial-cell density equation (1) and then the use of the resulting coefficients of the finite-difference stencil to generate the probabilities of movement of a single cell in response to its local environment. Since they used Euler's explicit forward time centered space scheme, using space-step lengths h in x- and y-directions and a time step of Δt resulted in the five point formula ([1]) is as follows:

$$n_{i,j}^{(n+1)} = P_0 n_{i,j}^{(n)} + P_1 n_{i+1,j}^{(n)} + P_2 n_{i-1,j}^{(n)} + P_3 n_{i,j+1}^{(n)} + P_4 n_{i,j-1}^{(n)} \tag{15}$$

where,

$$P_0 = 1 - \frac{4\Delta t D}{h^2} + \frac{\Delta t \alpha \chi\left(c_{i,j}^{(n)}\right)}{4h^2\left(1+\alpha c_{i,j}^{(n)}\right)}\left[\left(c_{i+1,j}^{(n)} - c_{i-1,j}^{(n)}\right)^2 + \left(c_{i,j+1}^{(n)} - c_{i,j-1}^{(n)}\right)^2\right]$$

$$- \frac{\Delta t \alpha \chi\left(c_{i,j}^{(n)}\right)}{4h^2}\left[\left(c_{i+1,j}^{(n)} + c_{i-1,j}^{(n)} - 4c_{i,j}^{(n)} + c_{i,j+1}^{(n)} + c_{i,j-1}^{(n)}\right)\right]$$
$$- \frac{\Delta t \rho}{4h^2}\left[\left(f_{i+1,j}^{(n)} + f_{i-1,j}^{(n)} - 4f_{i,j}^{(n)} + f_{i,j+1}^{(n)} + f_{i,j-1}^{(n)}\right)\right]$$

$$P_1 = \frac{\Delta t D}{h^2} - \frac{\Delta t}{4h^2}\left[\chi\left(c_{i,j}^{(n)}\right)\left(c_{i+1,j}^{(n)} - c_{i-1,j}^{(n)}\right) + \rho\left(f_{i+1,j}^{(n)} - f_{i-1,j}^{(n)}\right)\right]$$

$$P_2 = \frac{\Delta t D}{h^2} + \frac{\Delta t}{4h^2}\left[\chi\left(c_{i,j}^{(n)}\right)\left(c_{i+1,j}^{(n)} - c_{i-1,j}^{(n)}\right) + \rho\left(f_{i+1,j}^{(n)} - f_{i-1,j}^{(n)}\right)\right]$$

$$P_3 = \frac{\Delta t D}{h^2} - \frac{\Delta t}{4h^2}\left[\chi\left(c_{i,j}^{(n)}\right)\left(c_{i+1,j}^{(n)} - c_{i,j-1}^{(n)}\right) + \rho\left(f_{i,j+1}^{(n)} - f_{i,j-1}^{(n)}\right)\right]$$

$$P_4 = \frac{\Delta t D}{h^2} + \frac{\Delta t}{4h^2}\left[\chi\left(c_{i,j}^{(n)}\right)\left(c_{i+1,j}^{(n)} - c_{i,j-1}^{(n)}\right) + \rho\left(f_{i,j+1}^{(n)} - f_{i,j-1}^{(n)}\right)\right]$$

and the subscripts specify the location on the grid and the superscripts the time steps. That is $x = ih$, $y = jh$ and $t = n\Delta t$. By using the data generated from the numerical solution of equation (1), the discrete equation (15) determines the endothelial-cell density at $(i, j)^{\text{th}}$ space location at the current time level by taking the average of the densities of the $(i-1, j)^{\text{th}}$, $(i+1, j)^{\text{th}}$, $(i, j-1)^{\text{th}}$ and $(i, j+1)^{\text{th}}$ space locations at the previous time level.

Note that the scheme developed in section 3.3 is an implicit scheme which uses five points at the $(n+1)^{\text{th}}$ and nine points at the $(n)^{\text{th}}$ time level. As such a discrete model based on the proposed scheme should ideally involve nine coefficients involving the probability density function. Because of the implicitness of the scheme, the probability density functions must involve the effect of the coefficient matrix of the algebraic system of equations resulting from dicretization of the governing equations described in section 3.3 as well. However, devising such a mechanism is not an easy job, and the work on this is currently under progress by the authors. Moreover, this is a post-processing task involving the data accrued from the computation of the variables c and f, representing TAF and fibronectin concentrations respectively. As such, we have used the same five coefficients P_0-P_4 from equation (15) utilizing the data from our HOC computation to generate the movement of a single endothelial-cell. This strategy is justified under the assumption that these coefficients are directly proportional to the probabilities of the

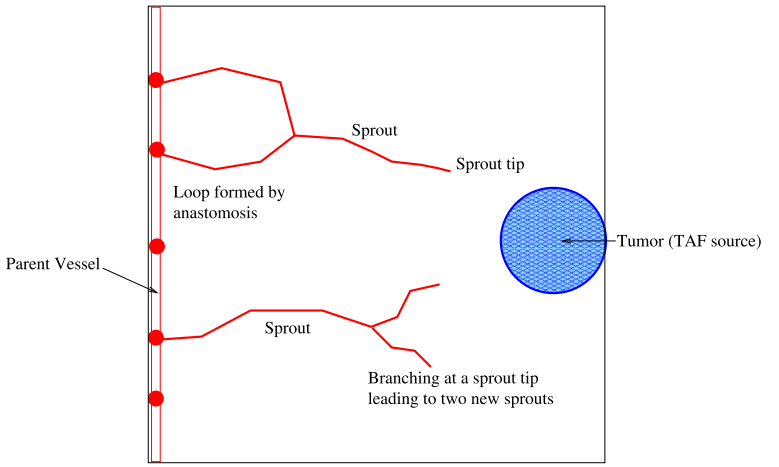

Figure 1: Schematic of branching: a capillary sprout tip producing two fresh sprouts and a loop formed by the anastomosis of two capillary sprouts.

endothelial cell, viz., stationary when probability is P_0 or moving up (P_3), down (P_4), left (P_1) or right (P_2).

As pointed out by Anderson and Chaplain [1], all the coefficients P_0-P_4 essentially consists of three vital components,

$$P_n = \textit{random movement} + \textit{chemotactic} + \textit{haptotatic} \tag{16}$$

demonstrating the connection between the discrete and the continuous system of equations (1).

Thus P_0-P_4 are functions of the fibronectin and TAF concentrations surrounding a single endothelial cell. As such the movement of the endothelial cells and the biasness of the coefficients towards the tumor source or any other direction depends on the amount of fibronectin and TAF gradients. The rules of branching and anastomosis used in the simulation is same as the ones used in Anderson and Chaplain [1]. The schematic diagram of Figure 1 shows how a capillary sprout tip produces two fresh sprouts and a loop is formed by the anastomosis of two capillary sprouts.

The probability density function mentioned above works in the following way: Once the five coefficients P_0-P_4 are known, probability ranges R_k, $0 \leq k \leq 4$ are estimated by summing up the coefficients by the formula $R_0 = -P_0$ and $R_i = \sum_{k=0}^{i-1} - \sum_{k=0}^{i}$, where $1 \leq i \leq 4$. Next, a random number lying between 0 and 1 is generated. Whether the individual cell under consideration will remain stationary (R_0), move towards left (R_1),

right (R_2), top (R_3) or bottom (R_4) is decided by the range into which this number falls [1].

5. Numerical simulations for the continuous model

In the previous sections we have already introduced the normalized set of partial differential equations (1) subject to boundary conditions (2). Wherever possible, the parameter values appearing in equations (1) have been chosen from the already available benchmark data. Based on the observations in [1, 17, 39, 47, 52], we assign the following set of values to our parameters

$$D = 0.00035, \quad \alpha = 0.6, \quad \chi = 0.38,$$
$$\gamma = 0.1, \quad h = 0.005, \quad \Delta t = 0.0001, \quad \text{and} \quad \eta = 0.1$$

In the following, we provide the results from our numerical simulations for the system of equation (1) from the continuous model, where we have primarily considered three cases. The first two corresponds to the time-space advancement of the endothelial-cell density mirroring the journey of endothelial-cell from the parent vessel towards tumor cell source in the shape of a line, once in the presence of haptotaxis and then without it. The last case deals with the same with a circular source of tumor cell in the presence of haptotaxis.

The initial conditions for the fibronectin concentration f (see figure 2(c)) and the endothelial-cell density distributions n (see figure 2(d)) for all the cases are respectively as follows

$$f(x, y, 0) = k\mathrm{e}^{-\frac{x^2}{\epsilon_2}}, \quad (x, y) \in [0, 1] \times [0, 1], \tag{17}$$

$$n(x, y, 0) = k\mathrm{e}^{-\frac{x^2}{\epsilon_3}} \sin^2(6\pi y), \tag{18}$$

while the initial conditions for the TAF concentration c (figure 2(a)) for the line source is taken as

$$c(x, y, 0) = \mathrm{e}^{-\frac{(1-x)^2}{\epsilon_1}}, \quad (x, y) \in [0, 1] \times [0, 1], \tag{19}$$

and that of the circular source (figure 2(b)) is [36]

$$c(x, y, 0) = \begin{cases} 1 & 0 \le r \le 0.1 \\ \frac{(v-r)^2}{(v-0.1)^2} & \text{otherwise} \end{cases} \tag{20}$$

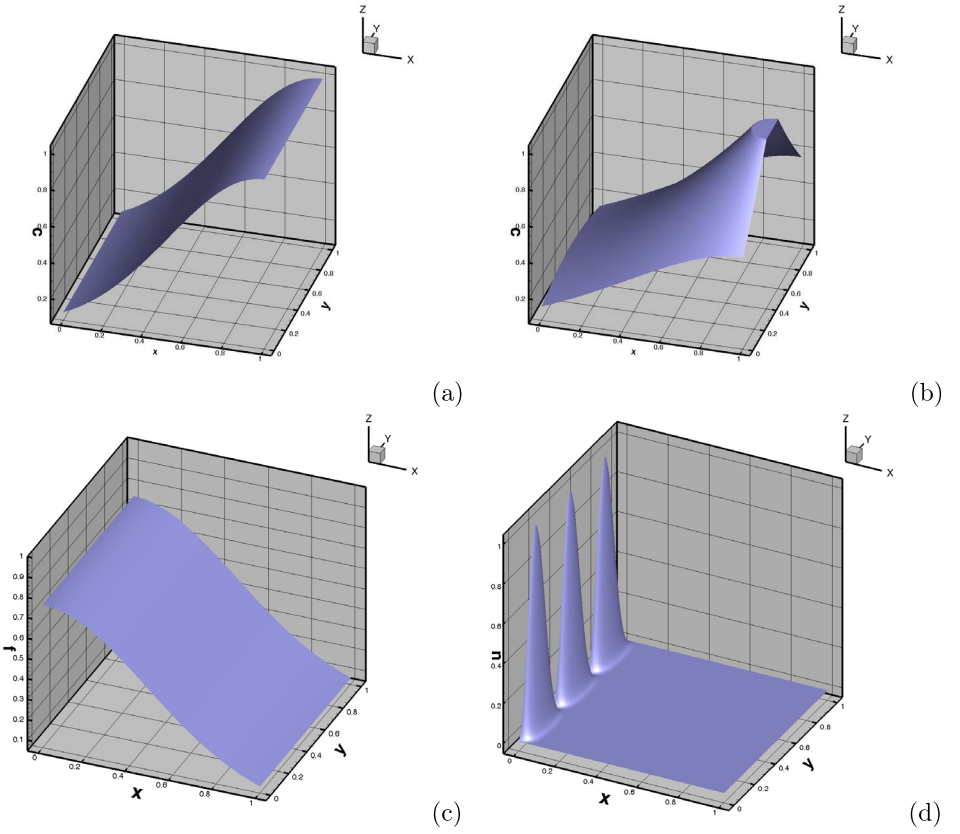

Figure 2: The initial TAF concentration for (a) the line and (b) the circular source, and the initial (c) fibronectin concentration and (d) endothelial cell density distribution.

with $v = \dfrac{\sqrt{5}-0.1}{\sqrt{5}-1}$ and $r = \sqrt{(x-1)^2 + \left(y - \dfrac{1}{2}\right)^2}$ $(x, y) \in [0,1] \times [0,1]$. For the current simulation, $\epsilon_1 = \epsilon_2 = 0.45$, and $\epsilon_3 = 0.001$ as in [1, 36]. Unless otherwise stated, all the simulations have been carried out on a grid size of 201×201.

5.1. Time-space advancement with a line source of tumor cells without haptotaxis

In the following, we present our results of the simulation without the presence of haptotaxis which corresponds to $\rho = 0$. The initial conditions are

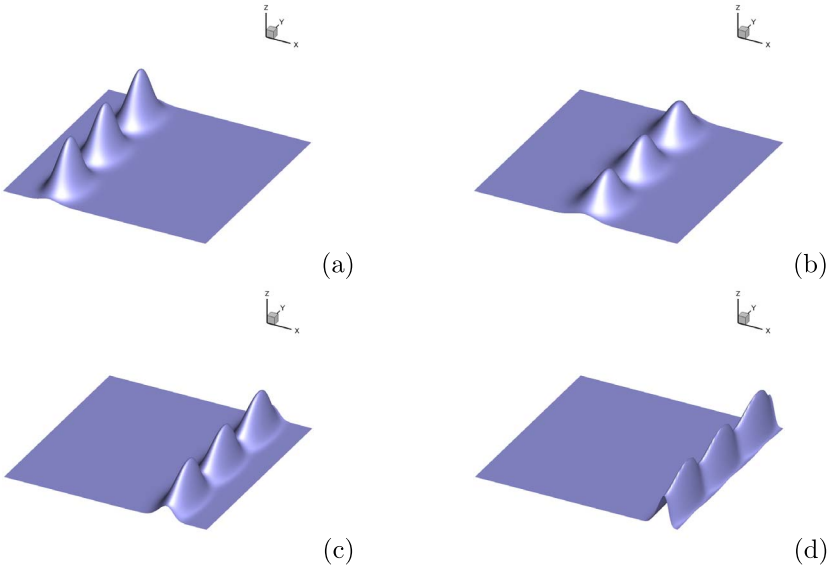

Figure 3: Surface plots of the time-space advancement of the density of endothelial-cell lacking haptotaxis with a line tumor cell source for (a) $t = 1$,(b) $t = 2$, (c) $t = 3$, and (d) $t = 4$.

as given by equations (17), (18) and (19), and depicted in figures 2(a), (c) and (d).

In Figure 3, we present the surface plots of the time-space advancement of the density of endothelial-cell in the absence of any haptotaxis resulting from our computation for the duration $t = 1$ to $t = 4$. The corresponding contour plots for the same duration are shown in Figure 4. From Figures 3(a)-(b), and 4(a)-(b), one can see that before reaching $t = 2$ (corresponding to 3 days) the endothelial cells have already swept aside over 50% of the domain, and by $t = 4$ (6 days) they have travelled through the whole domain. One crucial aspect of this migration is that there is hardly any movement of the endothelial cells parallel to the y-axis. One can also see that even after reaching the line source tumor cells, the shape of the surface of initial distribution represented by the three peaks is retained by the major chunk of the endothelial-cell density surface. This is owing to the fact that chemotaxis is dominant in controlling the movement of the cells with very little effect caused by random motility which is responsible for the lateral movement. We also compare our numerical results at times $t = 3$ and $t = 4$ with those of [1] in figures 4(c)-(d) and 4(e)-(f) respectively; one can see that they are very close to each other.

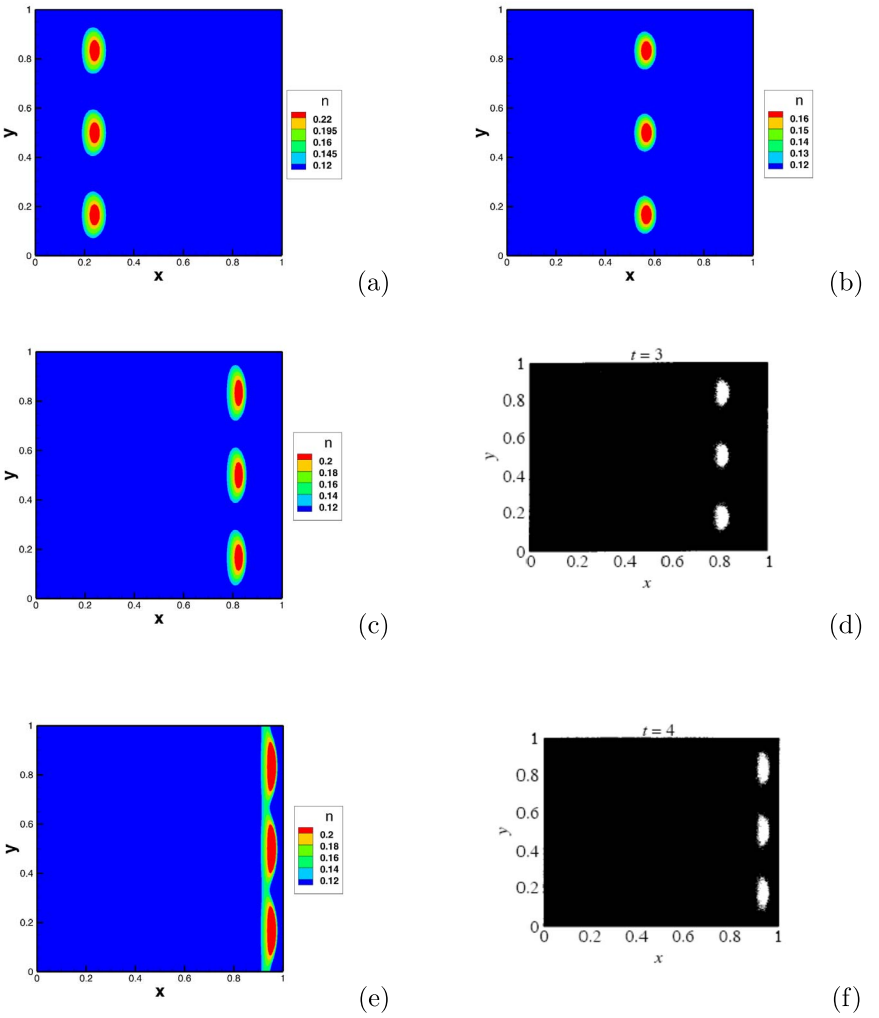

Figure 4: Time-space advancement of the density of endothelial-cell lacking haptotaxis in time and space ($\rho = 0$) at (a) $t = 1$,(b) $t = 2$, (c) $t = 3$, (d) $t = 3$ ([1]), (e) $t = 4$ and (f) $t = 4$ ([1]).

5.2. Time-space advancement with a line source of tumor cells with haptotaxis

Next, setting $\rho = 0.34$, we check the the significance of chemotaxis and haptotaxis on the endothelial-cell movement. In Figure 5, we present the surface plots of the time-space advancement of the density of of endothelial-

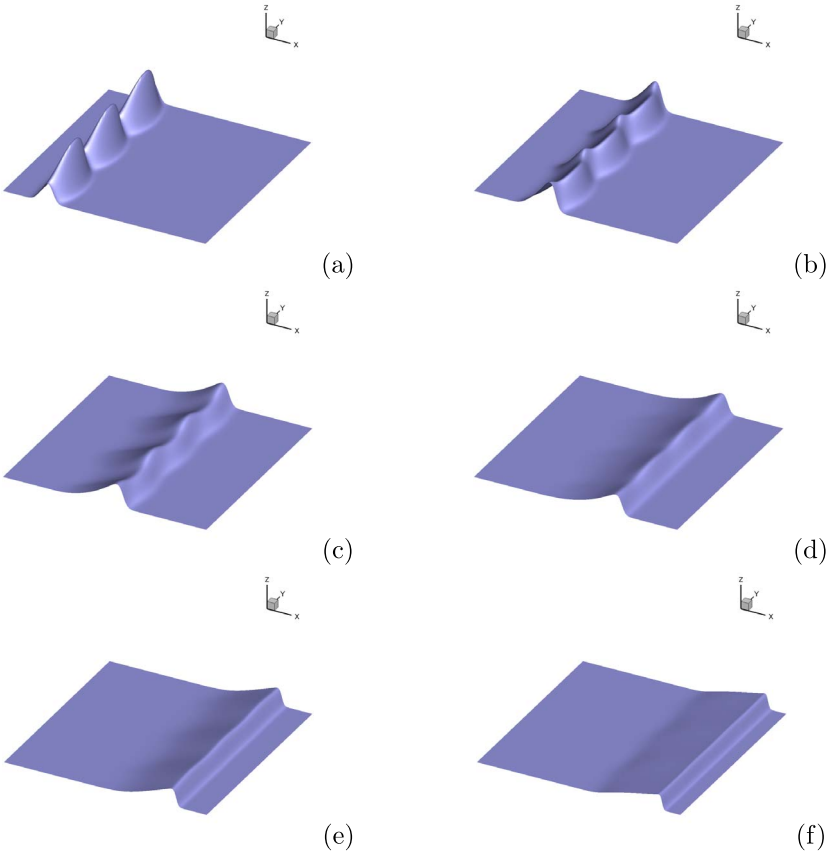

Figure 5: Surface plots of the time-space advancement of the density of endothelial-cell having both chemotaxis and haptotaxis from the parent vessel towards a line tumor cell source for (a) $t = 2$,(b) $t = 4$, (c) $t = 7$, (d) $t = 10$, (e) $t = 15$ and (f) $t = 20$.

cells for the duration $t = 2$ to $t = 20$ and the corresponding contour plots are shown in Figure 6. Once again the initial conditions are as in the previous example.

The surface plots from figures 3 and 4 clearly indicated that in the absence of haptotaxis, the three peaks during the entire course of evolution remained unattached throughout the whole the domain. On the other hand, in the presence of haptotaxis, the same bunches have merged with each other to form a continuous band even before $t = 4$ (see also figure 6(b)). At $t = 7$, one can see the presence of high concentration of endothelial cells at four

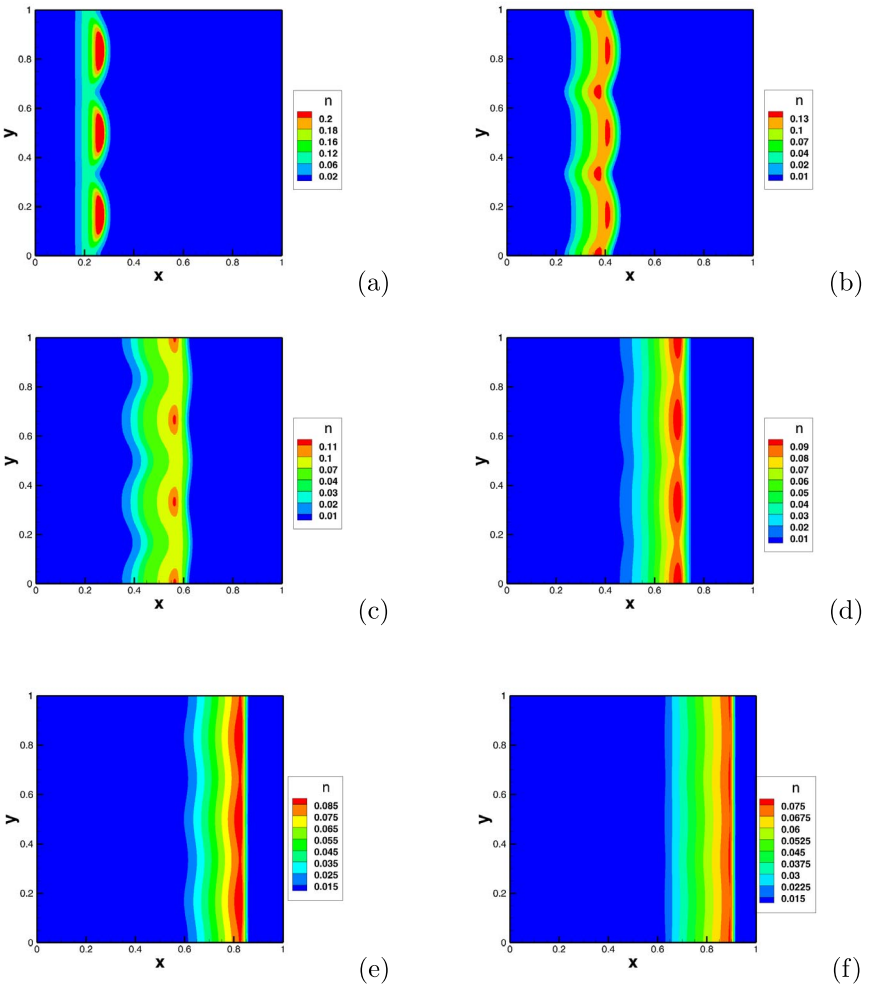

Figure 6: Time-space advancement of the density of endothelial-cell from HOC simulation in the presence of haptotaxis with $\rho = 0.34$ (a) $t = 2$, (b) $t = 4$, (c) $t = 7$, (d) $t = 10$, (e) $t = 15$ and (f) $t = 20$.

distinct locations (depicted by color red representing highest contour value in figure 6(c)) within the band. The initial peaks have overlapped with each other and there is clear evidence of parallel movement along y-axis now.

Another interesting observation here is that the movement of the cells towards the tumor is much slower than the previous case and also the circular shape of endothelial-cell density distribution as in figures 3 and 4 is no longer

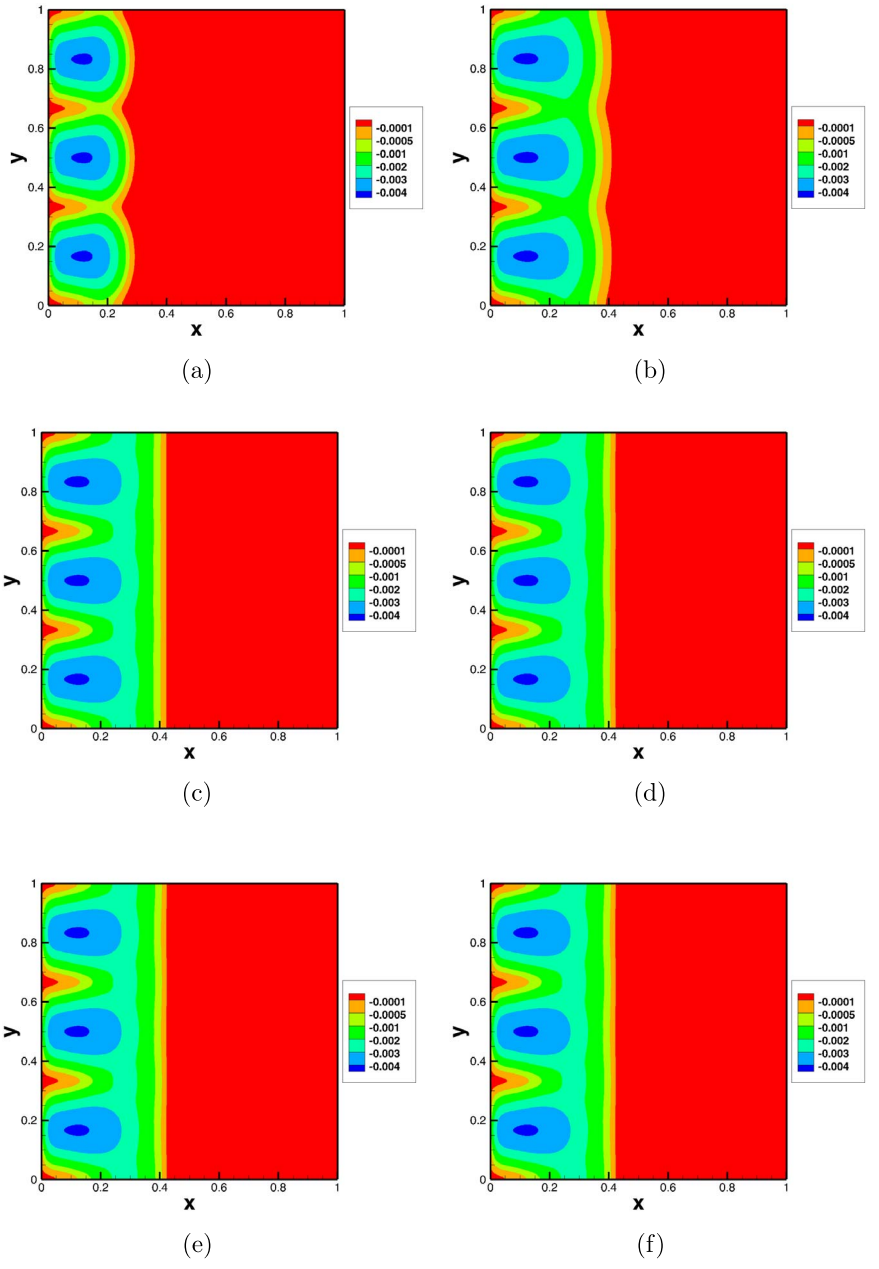

Figure 7: Initial and current fibronectin concentration differential of the fibronectin uptake at (a) $t = 2$, (b) $t = 4$, (c) $t = 7$, (d) $t = 10$, (e) $t = 15$ and (f) $t = 20$.

seen. The band is now more prominent at $t = 10$ (15 days) and stratified and gradually progressing toward the tumor in the presence of highest cell concentration at leading edge (figures 3(d)-(f) and 4(d)-(f)). However, the choice of the chemotactic function (χ in equation (1)) prevents the cells from reaching the tumor.

Figure 7 shows the difference in fibronectin concentration between the initial and current time at certain time junctures. The regions barring the red coloured ones are those having gained in fibronectin by the endothelial cells. This figure is a clear indication of the uptake process being confined in the first half of the entire domain $0 \leq x \leq 0.5$ and remaining almost invariant after $t = 7$. The behaviour of the endothelial cells in Figures 5 and 6 is a direct consequence of these fibronectin gradients formed in the extracellular matrix.

The panel on the right of each of the figures of 7 shows the contour values and as such indicates the gradation of these colours being directly proportional to the net uptake of fibronectin, enabling the the endothelial cells to move forward.

5.3. Time-space advancement with a circular source of tumor cells with haptotaxis

This case resembles the laboratory experiment of Muthukkarupan *et al.* [39], who implanted a spherical tumor in the cornea of a mouse in order to observe the angiogenic response. All the parameters and governing equations are as in the previous subsections except that the initial conditions are now as in equations (17), (18) and (20) which are depicted in figures 2(b)-(d). The distribution of TAF concentration resulting from a circular tumor implant (figure 2(b)) centered at $\left(1, \frac{1}{2}\right)$ and the value v of equation (20) is chosen in such a way that the continuity of the TAF concentration is maintained at $r = 0.1$ and the minimum value of c at $x = 0$ resulting from equations (19) and (20) are approximately the same.

In Figure 8, we show the surface plots of the time-space advancement of the density of endothelial-cells from the current simulation from the parent vessel towards a circular tumor implant. Compared to the line source tumor case, the response of the cells to the tumor implant is quite different here. A close look at figures 5(a)-(b) and 8(a)-(d) reveals that while in the former the clusters in the shape of crescent moved almost laterally, here at $t = 2$, the outer clusters have moved towards the central one. Moving along laterally, they merge to form two clusters at $t = 3$, which eventually form a

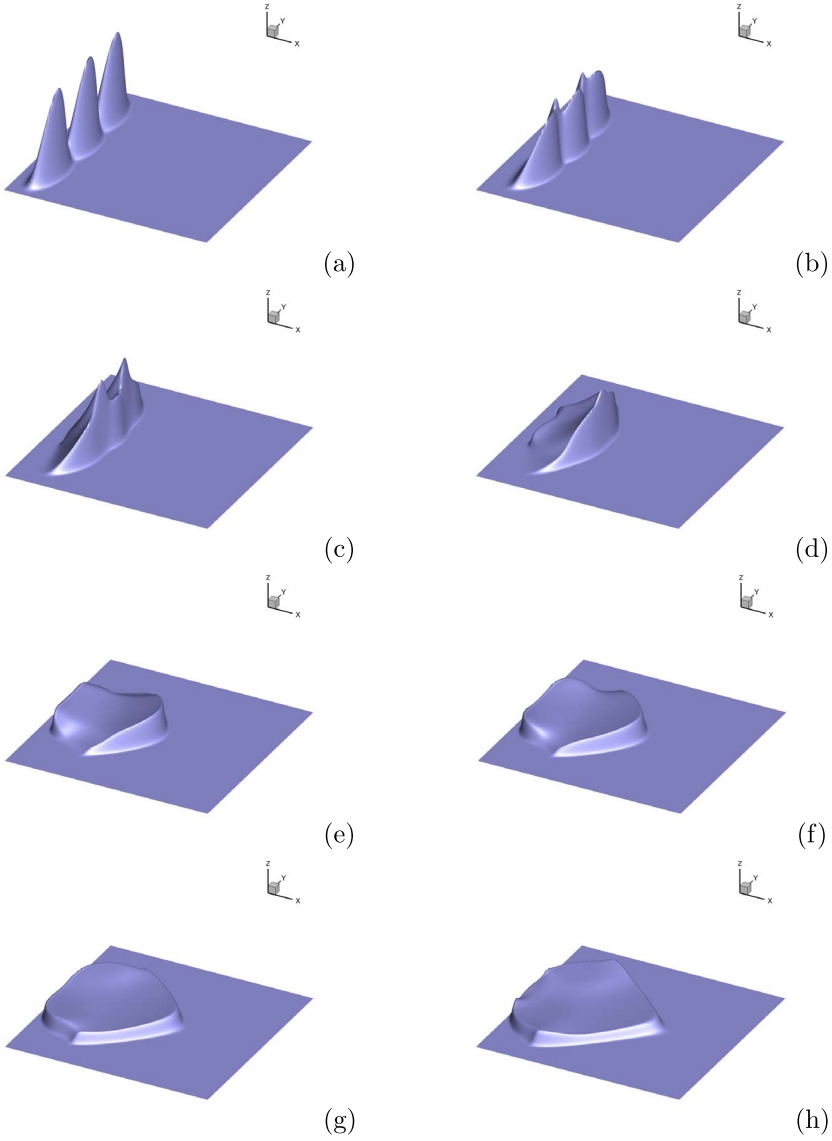

Figure 8: Surface plots of the time-space advancement of the density of endothelial-cell from the parent vessel towards a circular tumor cell from the current HOC simulation for (a) $t = 1$,(b) $t = 2$, (c) $t = 3$, (d) $t = 5$, (e) $t = 10$, (f) $t = 12$, (g) $t = 15$ and (h) $t = 18$.

single cluster at $t = 4$. Moreover, the movements of the clusters are much slower here as evidenced by the surface plots of both the cases at $t = 4$. Subsequently, one can also see both forward and backward migration of the cells (figures 8(e)-(h)) for this particular case. While we saw high density region at the forefront in the line source case, here they appear both at the forefront as well as near the parent vessel at $x = 0$ (figure 8(f)). The single cluster flattens, move both in lateral and transverse direction and due to its slow motion does not reach the source even at $t = 20$. Interestingly, while the simulations of Anderson and Chaplain [1] reported a small cluster of cells reaching the tumor, no such event was observed in our simulation. We shall discuss about this issue and present more simulation results for the later part of the physiological evolution in Section 7.

6. Discrete model simulation results

For the discrete model, in order to study the migration of the endothelial cells, initially five points (see figure 1 also) were chosen at the extreme left of the domain ($x = 0$). These five points represent the tips of capillary sprouts initiated the endothelial cells; three of them are assumed to be at the positions where the continuous endothelial-cell density is maximum at time $t = 0$ (data corresponds to figure 2(d)). The remaining two are exactly located midway through between the top and middle, and the middle and bottom. Thus, we have endothelial cells starting at $y = 0.17,\ 0.3,\ 0.5,\ 0.65,\ 0.84$ all at $x = 0$ (see figure 1). We present the same cases considered under the continuous model in sections 5.2 and 5.3, viz., the time-space advancement of the density of endothelial-cells in the presence of haptotaxis, once with a line source of tumor cells and then with a circular source. The initial and boundary conditions for both the cases are as in the continuous model.

6.1. Line source of tumor cells with haptotaxis

In Figure 9, we show the time-space advancement of a capillary network from the numerical simulation of the discrete model by our HOC scheme in the presence of haptotaxis. The figures show the journey of the endothelial cells at the capillary sprout tips starting at the parent vessel in the extreme left ($x = 0$) towards the extreme right ($x = 1$) where the line source of tumor cells is located. We also compare our results with those of [1] at later times. Initially at $t = 3$ (figure 9(a)), one can see a trace of branching occuring at the third sprout which eventually leads to anastomosis between the second and the third sprouts as can be see in Figure 9(b). As time elapses, the

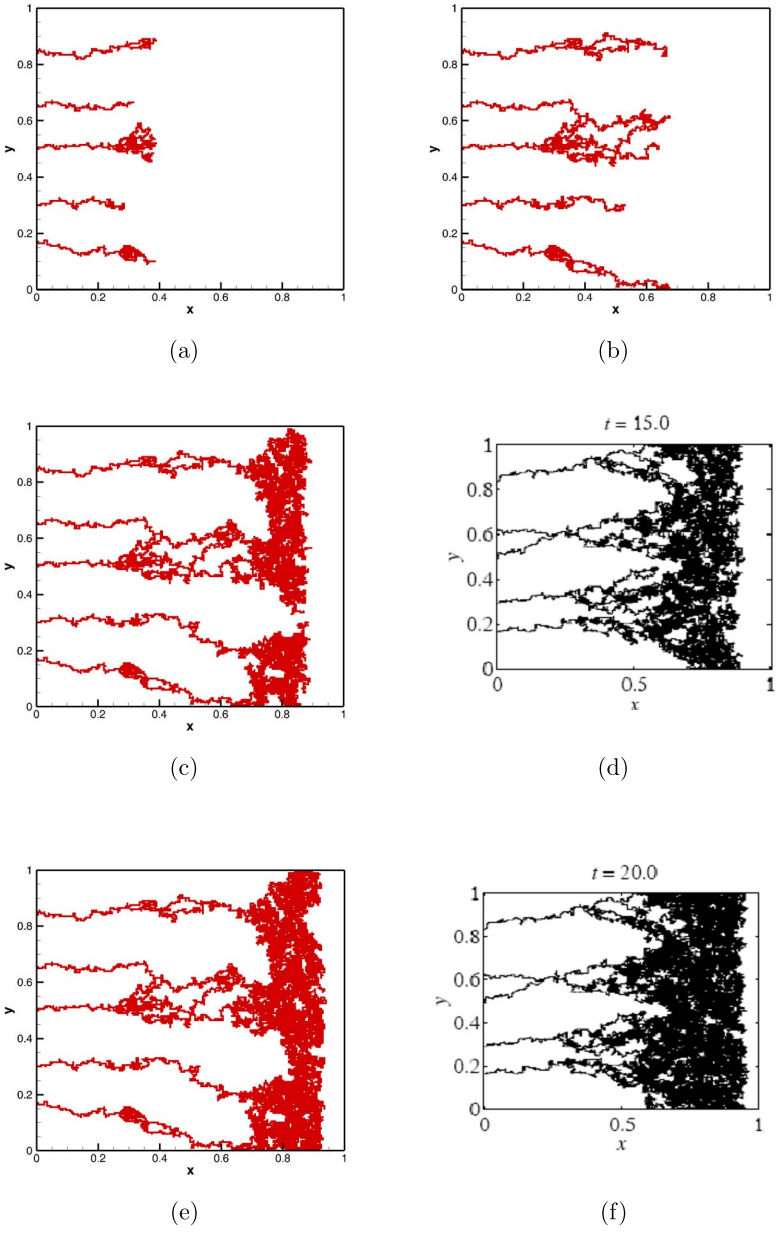

Figure 9: Space-time advancement of a capillary network from using data generated from HOC scheme for the discrete mathematical model for the line source at (a) $t = 3$,(b) $t = 7.5$, (c) $t = 15$, (d) $t = 15$ ([1]), (e) $t = 20$ and (f) $t = 20$ ([1]).

sprouts begin to branch and expand into the entire domain leading to the line tumor source (figures 9(c)-(f)). We have also compared our results with those obtained by Anderson and Chaplain [1] at times $t = 15$ and $t = 20$ in figures 9(c)-(d) and 9(e)-(f) respectively; the slight discrepancy one observes here between the two computations may be due to the data resulting from numerical schemes of different accuracies.

6.2. Circular source of tumor cells with haptotaxis

Next we move to the case of a circular tumor sitting in the extreme right of the domain. This case is a classic example of how the geometry of the tumor holding the TAF concentration influences the cell movement and capillary network formation. This is exemplified by Figure 10, where we show the time-space advancement of a capillary network from the current numerical simulation of the discrete model arising out of the circular source. One can clearly see from figure 10(a) that by $t = 3$, the sprouts have formed anastomosis with further indication of loop formation by itself. The backward movement of one of the sprouts towards the parent vessel and branching thereof is clearly visible from figures 10(a)-(b) which is corroborated by the profiles shown in Figures 8(a)-(d). Cell migration towards the tumor is much slower than the previous case of line tumor. At later time, one can observe the formation of brush-border structure as reported in [39, 53] (Figures 10(e)-(h)) which is characterized by a very dense distribution of the vessels at the front region encompassing the neighbourhood of the tumor compared to the rest of the domain. Our observation is in conjunction with the ones observed experimentally in neovascularization induced by mammary adenocarcinomas implant in the mouse cornea (Muthukkaruppan et al., [39]). A close match was obtained while comparing our results with those obtained by Anderson and Chaplain [1] at time junctures $t = 15$ and $t = 20$ in Figures 10(e)-(f) and 10(g)-(h) respectively.

7. Numerical issues and physiological misrepresentation

In this section we discuss the numerical issues related to the simulation of tumor induced angiogenesis and how the use of lower order accurate numerical schemes could end up showing misrepresented simulation of the actual process.

Note that in our computation with the HOC scheme, we have used spatial grids of size 101×101, 201×201, 301×301 and 401×401, and a time step of $\Delta t = 0.001$ for all the grids. In Figure 11(a), we show the contour plots of

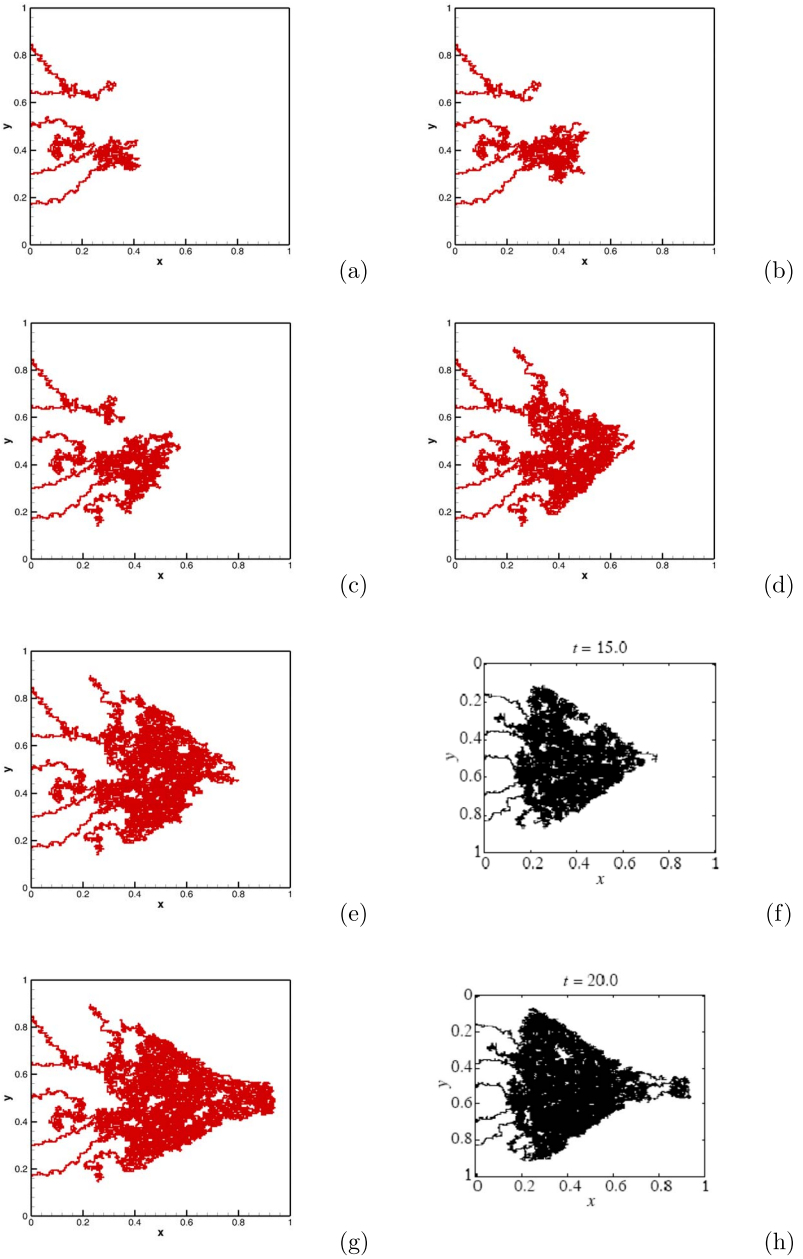

Figure 10: Space-time advancement of a capillary network from using data generated from HOC scheme for the discrete mathematical model for the circular source leading to brush border structure at (a) $t = 1$,(b) $t = 3$, (c) $t = 5$, (d) $t = 10$, (e) $t = 15$, (f) $t = 15$ ([1]), (g) $t = 20$ and (h) $t = 20$ ([1]).

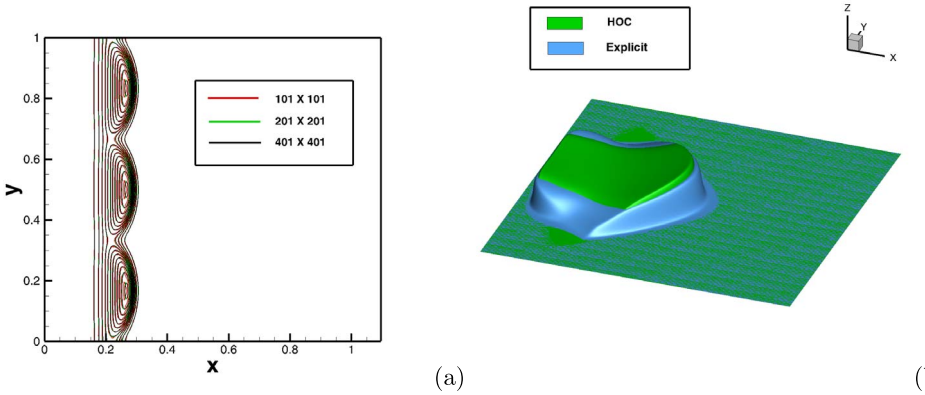

(a) (b)

Figure 11: (a) Grid independence study for the current scheme: contour plots of the endothelial cell density at time $t = 2$ on grids of size 101×101, 201×201 and 401×401 for a line source with haptotaxis, and (b) Surface plots of the endothelial cell density with a circular source at time $t = 10$ with the explicit and the HOC scheme.

the endothelial cell density at time $t = 2$ on grids of size 101×101, 201×201 and 401×401 for a line source with haptotaxis. One can clearly see that the contours are extremely close to each other in all grids, and particularly the contours are overlapping each other on the grids 201×201 and 401×401. Although a grid of size 101×101 was good enough to capture all the details of tumor induced angiogenesis, for a better resolution, all the results from our HOC computation shown here are on a grid of size 201×201. Only on figure 13, we have used a grid of size 301×301 in order to capture the details of the interaction of the circular tumor source and the endothelial cells in the later part of the process.

We have also numerically solved the governing equations using the Euler's explicit scheme as done by Anderson and Chaplain [1] and many other earlier studies (see [36, 54] also) in order to gain more insight of the numerical simulation process. Because of stability issues involved with explicit scheme, an extremely small time step $\Delta t = 10^{-5}$ had to be used on a grid of size 301×301 for the circular tumor source case. Even with Δt as small as this, the solution blew up after non-dimensional time $t = 5.12$, 9.93 and 17.22 on grids of size 101×101, 201×201, 257×257 respectively. In Figure 11(b), by superposing the surface plots of the endothelial density for the circular tumor case at $t = 10$, we compare the computed results by the explicit and HOC scheme. One can clearly see that the results from the explicit

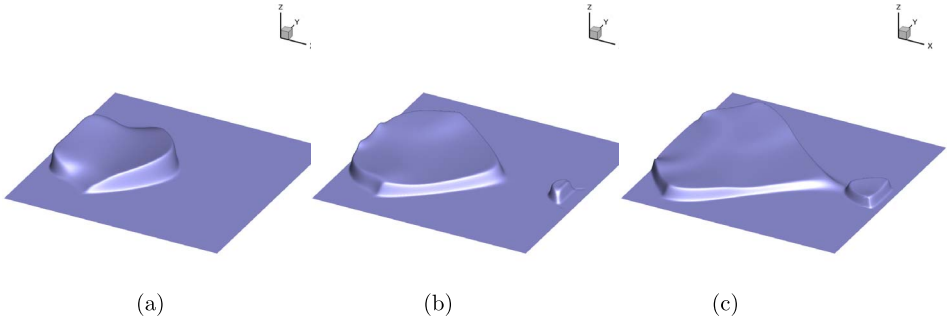

Figure 12: Surface plots of the space-time advancement of the density of endothelial-cells resulting from the explicit scheme mirroring the journey of endothelial cells from the parent vessel towards a circular tumor implant for (a) $t = 10$,(b) $t = 15$ and (c) $t = 20$.

scheme is over diffusive as evidenced by the lower height and extent of the surface for the explicit case.

Another very interesting observation resulting from the computation through the explicit and HOC scheme come into fore at the later stages of the endothelial cell migration. These are depicted in Figure 12 representing the surface plots resulting from the explicit scheme between time $t = 10$ and $t = 20$, and that from the HOC scheme between time $t = 20$ and $t = 30$ in figure 13. One can clearly see a cluster of endothelial cells around the source of the tumor at time $t = 15$ in Figure 12(b) in the form of a bulge; this however seems highly non-feasible as one can see complete detachment of the this small concentration and the part migrating originally from the parent cells. Figure 12(c) in isolation seems a more realistic one as it shows the endothelial cells migrating towards the center of the tumor and a small cluster forming around it. Anderson and Chaplain [1] reported that "at this stage interactions between the endothelial cells and the tumor cells is now important and our model is no longer valid". However, after computing the endothelial cell density by our HOC for a much longer period of time (see Figure 13), we strongly believe that the model is still very much valid, but the discrepancy in the actual representation of the fact by the explicit scheme is because of the presence inherent implicit numerical diffusion (and probably some implicit numerical dispersion also [24]) owing to its lower spatial and temporal accuracy.

It is heartening to note that the simulation from the HOC scheme is able to provide a more realistic picture of the situation. From Figures 13(a)-(f), it is clear that the HOC scheme has been able to capture the gradual

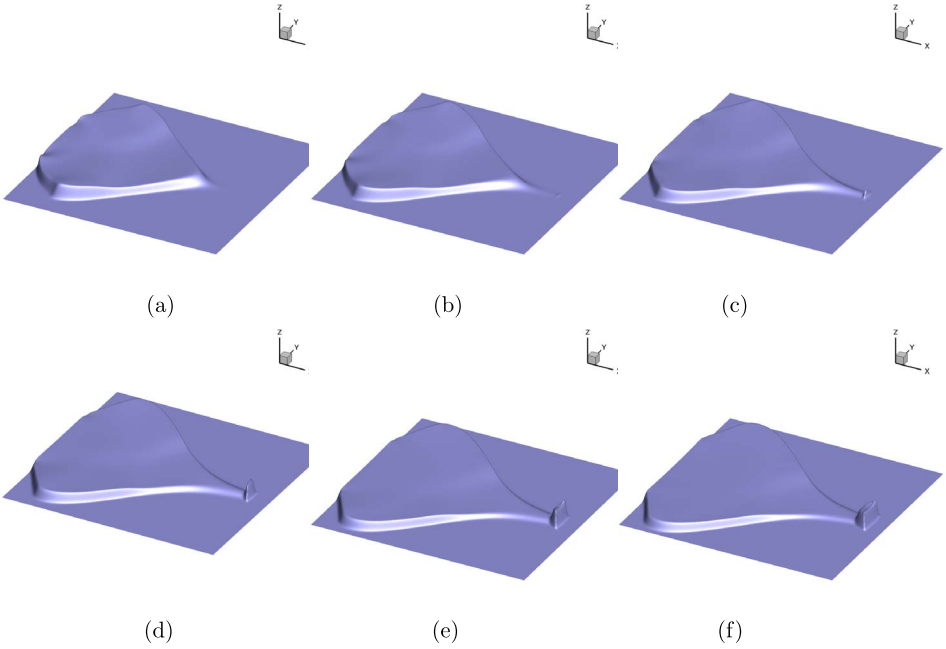

Figure 13: Surface plots of the space-time advancement of the density of endothelial-cells from the current simulation from the parent vessel towards a circular tumor implant for (a) $t = 20$,(b) $t = 22$, (c) $t = 24$, (d) $t = 26$, (e) $t = 28$ and (f) $t = 30$.

migration of the cells towards the tumor source finally culminating with interaction with it and producing a small cluster of endothelial cells around it. The results from the discrete model also corroborate the fact as one compares Figures 10(e)-(f) and 10(g)-(h). The brush border structure near the tumor resulting from our HOC computation is more prominent than the one computed by [1] using Euler explicit scheme.

8. Conclusions

In the current study, we have proposed a High Order Compact finite difference scheme for the tumor induced angiogenesis, more specifically for the equation governing the endothelial cell density evolution. Contrary to the earlier schemes that were employed to tackle such problems which were spatially second order accurate at the most and explicit in nature, the one proposed here is implicit, $O(\Delta x^4, \Delta y^4, \Delta t^2)$. Moreover, unconditional stability of the scheme enables a much larger time step to reach steady-state

or final time. In conjunction with a fourth order approximation of normal derivatives, the scheme was seen to tackle the no-flux Neumann boundary conditions with ease. To the best of our knowledge, an HOC approach for discretizing the equations for tumor induced angiogenesis has never been implemented before. In order to validate the scheme, we apply it to three pertinent problems. The first two corresponds to the time-space advancement of the density of endothelial-cells mirroring the migration of endothelial-cells from the parent vessel towards a line tumor cell source with and without haptotaxis. The last deals with the same with a circular source of tumor cell with haptotaxis. We compare our numerical results with available numerical and experimental ones and in all the cases, the match is excellent. The robustness of the scheme can be gauged from the fact that it accurately envisages the interaction between a circular tumor cell and the migrating endothelial cells in the later stages, which the Euler's explicit scheme fails to do so. We thus demonstrate in the process that simulation resulting from lower order accurate schemes might lead to misrepresentation of the physiological process owing to their over-diffusive nature. The current results are clear indications of the potential of the scheme for more efficient application to many problems of mathematical biology, specifically in the field of cancer research.

References

[1] A. R. A. Anderson and M. A. J. Chaplain. Continuous and discrete mathematical models of tumor-induced angiogenesis. *Bulletin of Mathematical Biology*, 60:857–900, 1998.

[2] D. A. Anderson, J. C. Tannehil and R. H. Pletcher. Computational Fluid mechanics and Heat Transfer. *Hemisphere Publishing Corporation, New York*, 1984.

[3] F. Arnold and D. C. West. Angiogenesis in wound healing. *Pharmac. Ther.*, 52:407–422, 1991.

[4] D. H. Ausprunk and J. Folkman. Migration and proliferation of endothelial cells in preformed and newly formed blood vessels during tumour angiogenesis. *Microvasc. Res.*, 14:53–65, 1977.

[5] D. Balding and D. L. S. McElwain. A mathematical model of tumour-induced capillary growth. *J. Theor. Biol.*, 114:53–73, 1985.

[6] J. C. Bowersox and N. Sorgente. Chemotaxis of aortic endothelial cells in response to fibronectin. *Cancer Res.*, 42:2547–2551, 1982.

[7] S. B. Carter. Haptotaxis and the mechanism of cell motility. *Nature*, 213:256–260, 1967.

[8] S. B. Carter. Principles of cell motility: the direction of cell movement and cancer invasion. *Nature*, 208:1183–1187, 1984.

[9] M. A. J. Chaplain and A. M. Stuart. A model mechanism for the chemotactic response of endothelial cells to tumour angiogenesis factor. *IMA J. Math. Appl. Med. Biol.*, 10:149–168, 1993.

[10] W. J. Cliff. Observations on healing tissue: A combined light and electron microscopic investigation. *Trans. Roy. Soc. Lond.*, B246:305–325, 1963.

[11] E. J. Duh, G. L. King, and L. P. Aiello. Identification of a vegf receptor (kdr/flk) promoter element which binds an endothelial cell-specific protein conferring endothelial selective expression. *Opthamol. Vis. Sci.*, 38:1124–1125, 1997.

[12] D. J. Dumont, G. Gradwohl, G. H. Fong, M. C. Puri, M. Gertsenstein, A. Auerbach, and M. L. Breitman. Dominant-negative and targeted null mutations in the endothelial receptor tyrosine kinase, tek, reveal a critical role in vasculogenesis of the embryo. *Genes Dev.*, 8:1897–1909, 1994.

[13] H. Enderling and M. A. J. Chaplain. Mathematical modeling of tumor growth and treatment angiogenesis. *Current Phermaceutical Design*, 20:1–7, 2014.

[14] J. Folkman. Tumor angiogenesis. *Adv. Cancer Res.*, 43:175–203, 1985.

[15] J. Folkman and M. Klagsbrun. Angiogenic factors. *Science*, 235:442–447, 1987.

[16] G. H. Fong, J. Rossant, M. Gertsenstein, and M. L. Breitman. Role of the flt-1 receptor tyrosine kinase in regulating the assembly of vascular endothelium. *Nature*, 376:66–70, 1995.

[17] M. A. Gimbrone, R. S. Cotran, S. B. Leapman, and J. Folkman. Tumor growth and neovascularization: an experimental model using the rabbit cornea. *J. Natln. Cancer Inst.*, 52:413–427, 1974.

[18] M. M. Gupta, R. M. Manohar and J. H. Stephenson, A single cell high order scheme for the convection-diffusion equation with variable coefficients. *Int. J. Numer. Methods Fluids*, 4:641–651, 1984. MR0754894

[19] M. M. Gupta, J. C. Kalita, A new paradigm for solving Navier-Stokes equations: streamfunction-velocity formulation. *J. Comput. Phys.* 207(1):52–68, 2005. MR2143582

[20] D. Hanahan. Signaling vascular morphogenesis and maintenance. *Science*, 227:48–50, 1997.

[21] E. Hatva, A. Kaipainen, P. Mentula, J. Jaaskelainen, A. Paetau, M. Haltia, and K. Alitalo. Expression of endothelial cell-specific receptor tyrosine kinases and growth factors in human brain-tumors. *Am. J. Pathol*, 146:368–378, 1995.

[22] W. F. Herblin and J. L. Gross. Inhibition of angiogenesis as a strategy for tumour-growth control. *Mol. Chem. Neuropath.*, 21:329–336, 1994.

[23] P. W. Hewett and J. C. Murray. Coexpression of flt-1, flt-4 and kdr in freshly isolated and cultured human endothelial-cells. *Biochem. Biophys. Res. Commun.*, 221:697–702, 1996.

[24] J. D. Hoffmann. Numerical methods for engineers and scientists. *Marcel Dekker Inc., New York, USA*, 2001.

[25] R. O. Hynes. Fibronectins. *Springer-Verlag: New York*, 1990.

[26] S. Johansson, S. Gustafson, and H. Pertoft. Identification of a fibronectin receptor specific for rat liver endothelial cells. *Exp. Cell Res.*, 172:425–431, 1987.

[27] J. C. Kalita, D. C. Dalal, A. K. Dass. A class of higher order compact schemes for the unsteady two-dimensional convection-diffusion equation with variable convection coefficients. *Int. J. Numer. Meth. Fluids*, 38:1111–1131, 2002. MR1899287

[28] J. C. Kalita and P. Chhabra. An improved $(9, 5)$ higher order compact scheme for the transient two-dimensional convection-diffusion equation. *International Journal for Numerical Methods in Fluids*, 51:703–717, 2007.

[29] J. C. Kalita and S. Sen. The $(9, 5)$ HOC formulation for the transient Navier-Stokes equations in primitive variable. *International Journal for Numerical Methods in Fluids*, 55:387–406, 2007. MR2352687

[30] C. T. Kelley. Iterative methods for linear and nonlinear equations. *SIAM: Philadelphia, PA*, 1995. MR1344684

[31] J. Lacovara, E. B. Cramer, and J. P. Quigley. Fibronectin enhancement

of directed migration of b16 melanoma cells. *Cancer Res.*, 44:1657–1663, 1984.

[32] M. Li, T. Tang, B. Fornberg, A compact fourth-order finite difference scheme for the steady incompressible Navier-Stokes equations. *International Journal for Numerical Methods in Fluids*, 20:1137–1151, 1995. MR1332439

[33] L. A. Liotta, C. N. Rao, and S. H. Barsky. Tumour invasion and the extracellular matrix. *Lab. Invest.*, 49:636–649, 1983.

[34] L. A. Liotta, G. M. Saidel, and J. Kleinerman. Diffusion model of tumor vascularization. *Bull. Math. Biol.*, 39:117–128, 1977.

[35] J. A. Madri and B. M. Pratt. Endothelial cell-matrix interactions: in vitro models of angiogenesis. *J. Histochem. Cytochem.*, 34:85–91, 1986.

[36] N. V. Mantzaris, S. Webb and H. G. Othmer. Mathematical modeling of tumor-induced angiogenesis. *Journal of Mathematical Biology*, 49:111–187, 2004. MR2145689

[37] J. B. McCarthy and L. T. Furcht. Laminin and fibronectin promote the directed migration of b16 melanoma cells in vitro. *J. Cell Biol.*, 98:1474–1480, 1984.

[38] B. Millauer, Wizigman-Voos, H. Schnürch, R. Martinez, N. P. H. Müller, W. Risau, and A. Ullrich. High-affinity vegf binding and developmental expression suggest flk-1 as a major regulator of vasculogenesis and angiogenesis. *Cell*, 72:835–846, 1993.

[39] V. R. Muthukkaruppan, L. Kubai, and R. Auerbach. Tumor-induced neovascularization in the mouse eye. *J. Natl. Cancer Inst.*, 69:197–242, 1982.

[40] N. Ortega, D. Dossantos, and J. Plouet. Activation of the vegf receptor flt-1 mediates corneal endothelial-cell migration permeability. *Invest. Optham. Vis. Sci.*, 37:417–418, 1996.

[41] N. Ortega and J. Plouet. Constitutive expression of the vegf receptor kdr/flk-1 in corneal endothelial-cell mediates their proliferation. *Vis. Res.*, 35:4217–4218, 1995.

[42] S. K. Pandit, J. C. Kalita, D. C. Dalal, A fourth-order accurate compact scheme for the solution of steady Navier-Stokes equations on non-uniform grids. *Computers and Fluids*, 37(2):121–134, 2007. MR2645516

[43] C. Patterson, M. A. Perrella, W. O. Endege, M. Yoshizumi, M. E. Lee, and E. Haber. Down-regulation of vascular endothelial growth-factor receptors by tumor-necrosis-factor-alpha in cultured human vascular endothelial-cells. *J. Clin. Invest.*, 98:490–496, 1996.

[44] N. Paweletz and M. Knierim. Tumor-related angiogenesis. *Crit. Rev. Oncol. Hematol.*, 9:197–242, 1989.

[45] G. Pettet, M. A. J. Chaplain, D. L. S. McElwain, and H. M. Byrne. On the role of angiogenesis in wound healing. *Proc. Roy. Soc. Lond.*, B263:1487–1493, 1996.

[46] J. P. Quigley, J. Lacovara, and E. B. Cramer. The directed migration of b-16 melanoma-cells in response to a haptotactic chemotactic gradient of fibronectin. *J. Cell Biol.*, 97:450–451, 1983.

[47] M. A. Rupnick, C. L. Stokes, S. K. Williams, and D. A. Lauffenburger. Quantitative analysis of human microvessel endothelial cells using a linear under-agarose assay. *Lab. Invest.*, 59:363–372, 1988.

[48] S. L. Schor, A. M. Schor, and G. W. Brazill. The effects of fibronectin on the migration of human foreskin fibroblasts and syrian hamster melanoma cells into three-dimensional gels of lattice collagen fibres. *J. Cell Sci.*, 48:301–314, 1981.

[49] M. M. Sholley, G. P. Ferguson, H. R. Seibel, J. L. Montour, and J. D. Wilson. Mechanisms of neovascularization. vascular sprouting can occur without proliferation of endothelial cells. *Lab. Invest.*, 51:624–634, 1984.

[50] G. L. G. Sleijpen and H. A. Van der Vorst. Hybrid bi-conjugate gradient methods for CFD problems. *Computational Fluid Dynamics Review*, 457–476, 1995.

[51] W. F. Spotz, G. F. Carey, High-order compact scheme for the steady stream-function vorticity equations. *International Journal for Numerical Methods in Engineering*, 38:3497–3512, 1995. MR1356346

[52] C. L. Stokes, M. A. Rupnick, S. K. Williams, and D. A. Lauffenburger. Chemotaxis of human microvessel endothelial cells in response to acidic fibroblast growth factor. *Lab. Invest.*, 63:657–668, 1990.

[53] S. Tong and F. Yuan. Numerical simulations of angiogenesis in the cornea. *Microvasc. Res.*, 61:14–27, 2001.

[54] G. Valinova, I. Colonimas and H. Gomez. Capillary networks in tumor angiogenesis: From discrete endothelial cells to phase-field averaged descriptions via isogeometric analysis. *International Journal for*

Numerical Methods in Biomedical Engineering, 29(10):1015–1037, 2013. MR3118788

[55] D. F. Zawicki, R. K. Jain, G. W. Schmid-Schoenbein, and S. Chien. Dynamics of neovascularization in normal tissue. *Microvasc. Res.*, 21:27–47, 1981.

[56] X. Zheng and T. Jackson. A cell-based model of endothelial cell migration, proliferation and maturation during corneal angiogenesis. *Bulletin of Mathematical Biology*, 72:830–868, 2010. MR2609391

[57] http://www.ssisc.org/lis, 2013.

Jiten C. Kalita
Department of Mathematics
Indian Institute of Technology
Guwahati
India
E-mail address: jiten@iitg.ac.in
URL: www.iitg.ac.in/jiten

Shubham Goyal
Department of Mathematics
Indian Institute of Technology
Guwahati
India
E-mail address: shubhamgoyal022@gmail.com

Utkarsh Dixit
Department of Mathematics
Indian Institute of Technology
Guwahati
India
E-mail address: utkarsh.dixit11@gmail.com

Received July 31, 2019